The Astrophysical Journal, 693:713–721, 2009 March 1 doi:10.1088/0004-637X/693/1/713

SPITZER SPECTRAL MAPPING OF SUPERNOVA REMNANT CASSIOPEIA A

J. D. T. Smith[1,2], Lawrence Rudnick[3], Tracey Delaney[4], Jeonghee Rho[5], Haley Gomez[6], Takashi Kozasa[7], William Reach[5], and Karl Isensee[3]
[1] Ritter Astrophysical Observatory, University of Toledo, Toledo, OH 43606, USA; jd.smith@utoledo.edu
[2] Steward Observatory, University of Arizona, Tucson, AZ 85721, USA
[3] Astronomy Department, University of Minnesota, Minneapolis, MN 55455, USA
[4] Massachusetts Institute of Technology, Kavli Institute for Astrophysics and Space Research, Cambridge, MA 02139, USA
[5] *Spitzer* Science Center, Caltech, Pasadena, CA 91125, USA
[6] School of Physics and Astronomy, Cardiff University, Queens Buildings, The Parade, CF24 3AA, UK
[7] Department of Cosmosciences, Graduate School of Science, Hokkaido University, Sapporo 060-0810, Japan
Received 2008 August 1; accepted 2008 October 15; published 2009 March 3

ABSTRACT

We present the global distribution of fine-structure infrared line emission in the Cassiopeia A supernova remnant using data from the *Spitzer Space Telescope*'s infrared spectrograph. We identify emission from ejecta materials in the interior, prior to their encounter with the reverse shock, as well as from the postshock bright ring. The global electron density increases by $\gtrsim 100$ at the shock to $\sim 10^4$ cm^{-3}, providing evidence for strong radiative cooling. There is also a dramatic change in ionization state at the shock, with the fading of emission from low-ionization interior species like [Si II] giving way to [S IV] and, at even further distances, high-energy X-rays from hydrogenic silicon. Two compact, crescent-shaped clumps with highly enhanced neon abundance are arranged symmetrically around the central neutron star. These neon crescents are very closely aligned with the "kick" direction of the compact object from the remnant's expansion center, tracing a new axis of explosion asymmetry. They indicate that much of the apparent macroscopic elemental mixing may arise from different compositional layers of ejecta now passing through the reverse shock along different directions.

Key words: infrared: general – supernova remnants – supernovae: individual (Cassiopeia A) – X-rays: ISM

Online-only material: color figures

1. INTRODUCTION

Supernova remnant Cassiopeia A (Cas A) is both nearby (3.4 kpc) and very young (∼330 yr; Fesen et al. 2006), giving it a bright, richly detailed ejecta structure which has led to intensive study at many wavelengths, from gamma rays to radio (Rudnick 2002; Albert et al. 2007). Spectroscopy of distant light echoes from the original blast indicates that Cas A was the type IIb core collapse of a $\sim 15\ M_\odot$ main-sequence star (Krause et al. 2008), which models indicate are highly stratified, having lost a significant portion of the original outer layers of hydrogen and helium prior to collapse in stellar winds (Woosley et al. 1987). An initial outgoing "forward" shock wave driven by the blast is seen as a thin X-ray edge (Gotthelf et al. 2001) expanding at ∼5000 km s^{-1}, with a reverse shock being driven back into the outgoing ejecta as it interacts with circumstellar material and the interstellar medium, expanding at roughly half the rate of the forward shock (DeLaney & Rudnick 2003).

The high-resolution available ($1'' = 0.016$ pc) makes Cas A ideal for tracking the physical conditions in the layered ejecta material, following nucleosynthesis both before and during the supernova explosion, the subsequent mixing and inhomogeneous transport of the ejected materials, and the formation of dust in situ. The mid-infrared (MIR) is an ideal wavelength for studying these processes, as it is minimally affected by the significant line of sight dust extinction ($A_V = 4.6$–6.2; Hurford & Fesen 1996), and probes a rich suite of abundant ionized species including Si, S, Ne, and Ar which range in ionization energies from 8 to 100 eV. Previous MIR studies of the remnant using *Infrared Space Observatory* (*ISO*) mapping placed constraints on the dust formation and the appearance of macroscopic mixing of materials (Lagage et al. 1996; Douvion et al. 1999), and explored the velocity shifted line and dust emission in various regions using high-resolution MIR spectroscopy(Arendt et al. 1999).

We report on the first large, sensitive infrared spectral maps of the remnant, obtained by the *Spitzer Space Telescope* (Werner et al. 2004). The distribution of interstellar material, ejecta, and shocked circumstellar material is shown in the 24 μm maps of Hines et al. (2004). A model of the composition and mass of emitting dust associated with the remnant using this MIR data set was undertaken by Rho et al. (2008). Ennis et al. (2006) highlighted the associated deep 3.6–8 μm *Spitzer* IRAC imaging, exploring the survival of the various nuclear burning layers. Here, we present the distribution of the global fine structure infrared emission lines and constrain conditions in the emitting environments over the full remnant. The complex Doppler velocity field as traced by these fine-structure lines will be detailed separately (T. DeLaney et al. 2009, in preparation).

2. OBSERVATIONS AND REDUCTION

Low-resolution 5–38 μm spectral maps were obtained in 2005 January with the Infrared Spectograph (IRS; Houck et al. 2004) aboard *Spitzer*. A single mapping observation consisting of 364 individual rastered spectra was obtained in the long-low module (LL; 15–38 μm), utilizing $5\farcs08$ steps across the slit (1/2 slit width), and $158''$ steps along the slit (approximately the full subslit length), for a total of 12.6 s per position. Short-low (SL; 5–15 μm) coverage was obtained by tiling four separate spectral maps to accomodate the maximum observation duration limits of the IRS, comprising 1218 total independent spectra. Precise scheduling was required to fully tile the remnant without

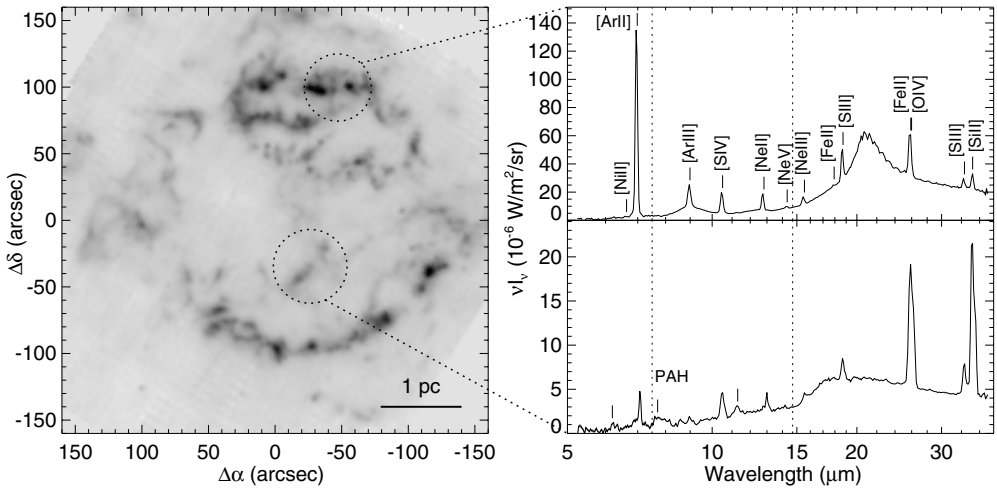

Figure 1. Left: full 7.5–14.7 μm map created from the SL1 cube, 320″×320″, square root scaled, with offset positions labeled relative to the expansion center (23:23:27.77, 58:48:49.4; Thorstensen et al. 2001). Representative spectra extracted in circular apertures are shown at right. Lines detected from the ejecta are labeled on the spectrum of the bright northern rim at top, and residual PAH features associated with the Galactic foreground are indicated on the much fainter interior emission spectrum below. Broad peaks at 9 and 21 μm are due to dust emission (see Rho et al. 2008), and the periodic signal at 20–25 μm is instrumental fringing. The wavelength range used to construct the map is indicated with vertical dotted lines.

allowing gaps to open between the quadrants. The SL slit was stepped at 2″×52″, for slightly less than double coverage and an effective exposure time of 11.4 s per position. The best effective resolution is ∼2″ in SL and ∼8″ in LL (varying linearly with wavelength). The total angular coverages obtained were 11.′0×7.′8 (LL) and 6.′3 × 5.′9 (SL).

Background removal was performed in situ, using spectral pointings selected from the periphery of the maps, choosing regions with low relative 24 μm surface brightness. Since the IRS subslits (mapped to separate grating orders) are separated by 180″ (LL) and 68″ (SL), multiple positions outside the main remnant are obtained in the course of a full spectral map in both orders, which aids in selecting suitable background spectra. However, since Cas A lies close to the Galactic plane, foreground and background emission from intervening and background Galactic cirrus clouds—including molecular hydrogen, polycyclic aromatic hydrocarban (PAH) emission, and weak low-ionization emission lines—is present throughout the region. This complex filamentary emission, readily seen in extended 24 μm maps (Kim et al. 2008), varies considerably over the face of the remnant, and is also present in the selected background regions. Although the contaminating line emission is very faint—$\lesssim$ 2% of the line surface brightness of the bright emitting ring—it provides a modest limitation on our ability to recover fluxes for the lowest surface brightness lines (see also Figure 1).

All IRS data were reduced from pipeline version S17 data products with Cubism, a custom tool created for the assembly and analysis of spatially resolved spectral cubes from IRS spectral maps (Smith et al. 2007). A total of four separate spectral cubes were created, one each for orders 1 and 2 of both SL and LL. The flux calibration was achieved using appropriate extended-source FLUXCON corrections, and aberrant or "rogue" pixels were automatically cleaned using the statistical methods built into Cubism, with a small amount of additional manual removal. The short 6.3 s exposure ramps contain only four samples, which leads to occasional anamolous cosmic ray correction, inducing small bad pixel clusters. These were mitigated with statistical record-level bad pixel flagging.

3. SPECTRAL MAPS

A full 7.5–14.7 μm map created from SL order 1 is shown in Figure 1, and offers excellent correspondence with the 8 μm IRAC map of Ennis et al. (2006). Two representative full spectra extracted from the interior and along the bright northern rim are also shown. These two spectra highlight the large dynamic range of line intensity, line ratios, and continuum shape across the remnant face. The broad peaks at 9 and 21 μm arise from warm protosilicate and other dust emission (see Rho et al. 2008).

Surface brightness maps from the eleven brightest emission lines (readily seen in Figure 1) are shown in Figure 2. Spectral line maps were created by integrating the spectral cube intensities over a wavelength region large enough to sample the line flux at all velocities present within the remnant (roughly −5000 km s^{-1} to +7000 km s^{-1}; see T. DeLaney et al. 2009, in preparation). Prior to integration, the local dust and synchrotron continuum emission was removed by subtracting a weighted average of flanking wavelength regions, carefully chosen to avoid contamination by nearby lines at all velocities. The averaging weight used at each wavelength within the line region ($\lambda_{\rm line}$) for a given continuum wavelength ($\lambda_{\rm cont}$) was $|\lambda_{\rm cont} - \lambda_{\rm line}|^{-1}$.

The broad dust feature present throughout most of the ejecta has a sharp peak at 21 μm, which induces a steep and variable continuum in the 15–21 μm range (see Figure 1). Estimating accurate line map fluxes in this range (LL order 2) required a preliminary continuum removal step. The cube was first smoothed spatially by three pixels. A linear or quadratic background function at each (smoothed) spatial position was fitted using two to four wavelength intervals free of line contamination, separately chosen for each line in the range. This noiseless background estimate was removed from the unsmoothed cube, and flanking continuum regions were then subtracted as above to eliminate any residual continuum contributions underlying the line. For the faint [Fe II] 17.94 μm line in this region, uncertainty in the continuum subtraction dominates the residual systematic errors.

Table 1 lists the lines detected at low resolution, with the peak surface brightness along the bright ring, as well as integrated line flux over the entire remnant. Very faint lines known to be associated primarily with Galactic cirrus emission, including

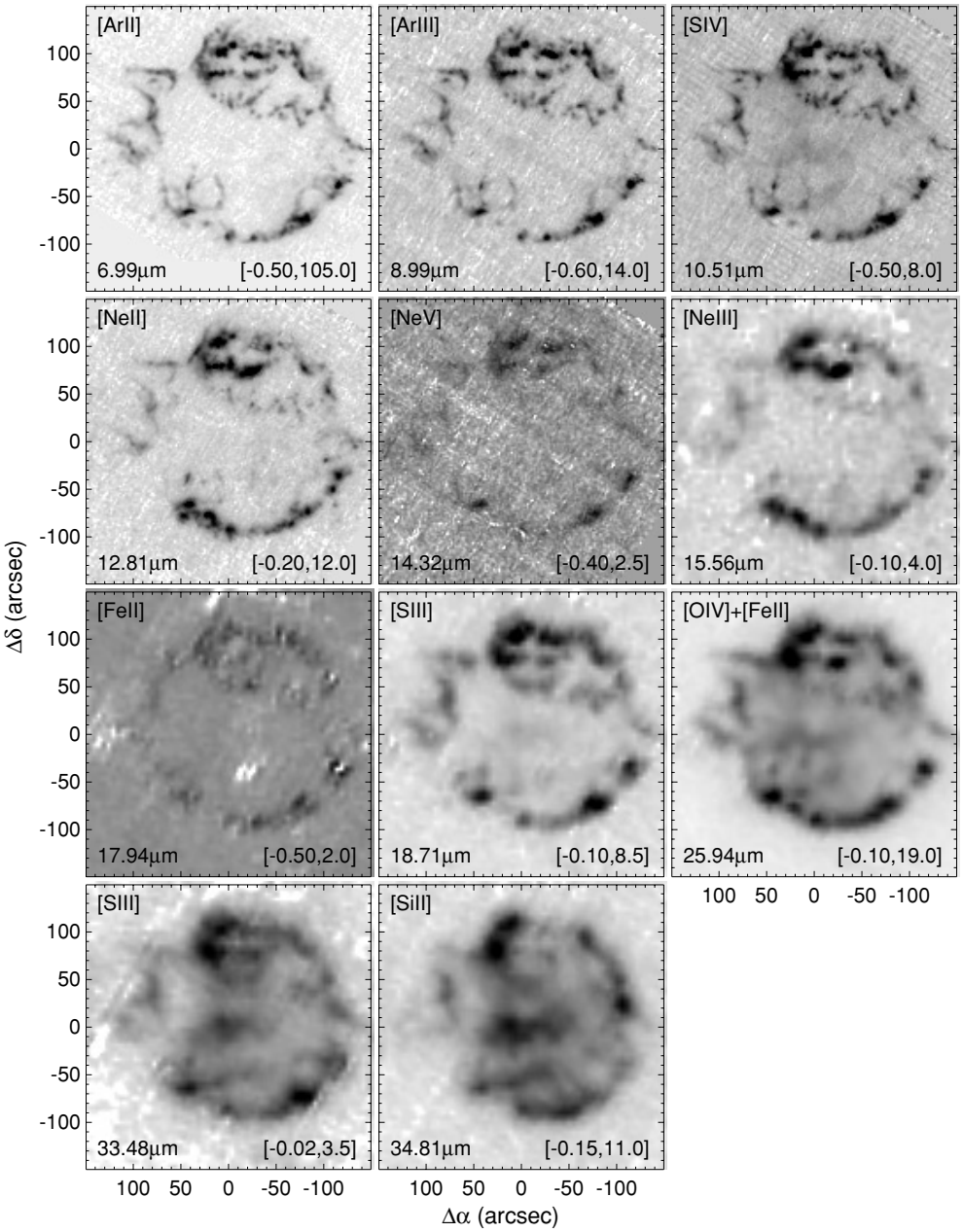

Figure 2. Surface brightness maps in the eleven brightest emission lines, sorted by order of increasing wavelength. Each image is 300″ × 300″, with offset positions as in Figure 1. The integrated, continuum-subtracted line surface brightness is square root scaled between low and high thresholds specified in brackets in each pane (in units of 10^{-7} W m^{-2} sr^{-1}).

rotational H_2 S(0)–S(2) and PAH emission features, are omitted, as are the integrated flux measurement of the faintest ejecta lines, which would be dominated by systematic errors. Among the brighter lines, systematic uncertainties in the total flux are 10% or less. Signal to noise in the brightest regions of the line maps was typically 30 or above. [Ar II] is by far the brightest line detected, and as it also offers the best spatial resolution, has proven very useful for Doppler decomposition of the remnant.

In many cases, line identification is hampered by Doppler broadening and, less frequently, multiple line-of-sight velocity components. The [O IV] line at 25.89 μm is a special example of such a case, as it is profoundly blended with [Fe II] 25.99 μm even at high spectral resolution. The line map at 26 μm therefore contains contributions from both of these lines. Constraints on the fractional contribution of [Fe II] and [O IV] in different regions can be made using expected line ratios to other lines of Fe, including [Fe II] 17.94 μm, as well as [Fe III] 22.93 μm, detected in our follow-on high-resolution maps of selected regions. Such an analysis will be considered in a subsequent study, but is consistent with both [Fe II] and [O IV] contributing and in differing amounts across the remnant.

In cases where Doppler confusion could support more than one line identification (most significant at the remnant center), we used our high-resolution spectra to resolve the ambiguity. An example for [Si II] is given in Figure 3. A consistent set of three velocity components is visible for [S III], [Si II], and a faint [Fe II] line undetected in our low-resolution data set.

A bright ring of emission, with overlapping smaller subrings most clearly seen in the north and southwest, is the dominant structure evident in all line maps, but significant

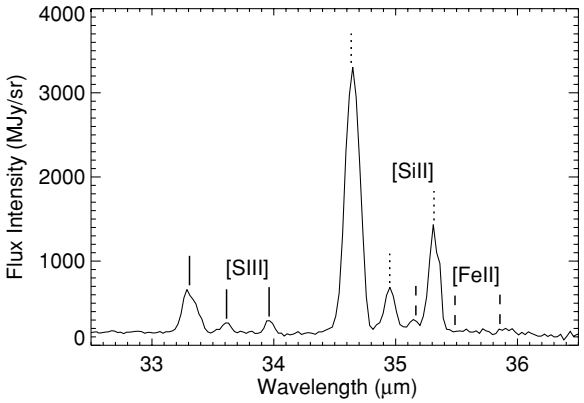

Figure 3. Portion of the high-resolution IRS spectrum of the central remnant, used to identify [Si II] emission at 35.3 μm. The [S III] 33.48 μm line was used to fit three velocity components at −1549, 1175, and 4303 km s^{-1}. These three components are marked for [S III] (solid lines), [Si II] (dotted), and a weak line of [Fe II] not detected in our low-resolution data set (dashed).

Table 1
Detected Emission Lines

Line	Wavelength (μm)	Peak Intensity (10^{-7} W m^{-2} sr^{-1})	Total Flux (10^{-13} W m^{-2})
(1)	(2)	(3)	(4)
[Ni II]	6.636	2.4 ± 0.85	...
[Ar II]	6.985	221. ± 0.86	7.72
[Ar III]	8.991	41.7 ± 0.82	1.24
[S IV]	10.511	21.0 ± 0.43	1.17
[Ne II]	12.814	33.7 ± 0.21	1.41
[Ne V]	14.322	1.75 ± 0.17	...
[Ne III]	15.555	8.62 ± 0.17	0.49
[Fe II]	17.936	2.49 ± 0.14	...
[S III]	18.713	13.2 ± 0.23	1.44
[O IV][a]	25.890	27.1 ± 0.29	4.95
[Fe II][a]	25.988	...	...
[S III]	33.481	4.08 ± 0.18	1.02
[Si II]	34.815	12.3 ± 0.21	3.16

Notes. Column 1: line name; Column 2: rest wavelength; Column 3: peak surface brightness over 1.″85^2 (SL) and 5.″08^2 (LL) areas; Column 4: total flux integrated over the remnant in a 5.′3 × 5.′3 region; statistical uncertainties in the total are 0.01 or less in these units. Faint lines excluded.
[a] [O IV] and [Fe II] are blended into a single emission peak at LL resolution.

variations in the line strengths occur throughout, in particular when comparing the interior to the ring. For the most part, the line strength variations on the bright ring are not complicated by the three-dimensional structure of Cas A. This is apparent in the Doppler reconstruction of Lawrence et al. (1995) which shows that there are very few overlapping structures along the same line of sight, with the exception of the north–northeast and the base of the northeast jet. The same cannot be said of the interior emission, where nearly every line of sight has two or more dominant Doppler components (T. DeLaney et al. 2009, in preparation).

4. PROGRESSION OF THE SHOCK

A reverse shock driven by the interaction of high velocity ejecta with the circumstellar material is propagating backwards into the outflowing material at a speed of 2500–4400 km s^{-1} (relative to the bulk outflow velocity; DeLaney & Rudnick 2003; Morse et al. 2004). Material inside the reverse shock boundary was "once-shocked" by the initial outgoing blast wave, but has subsequently cooled and recombined, and has not yet been reheated and reionized by the returning reverse shock. Three-dimensional Doppler reconstructions of optical and infrared lines such as [Ar II] show that they illuminate the reverse shock in a broad band approximately in the plane of the sky, forming the bright ring (Lawrence et al. 1995; also see T. DeLaney et al. 2009, in preparation). There is little or no emission from these ring lines across the face of the remnant; however, interior to the ring, strong emission lines of the low ionization species of S and Si appear. The velocity distribution of the interior [Si II] emission, shown in Figure 4, demonstrates that this central material lies fully inside the reverse shock boundary. In addition to these lines, strong 26 μm emission is present in the interior, contributed by [Fe II] and/or [O IV].

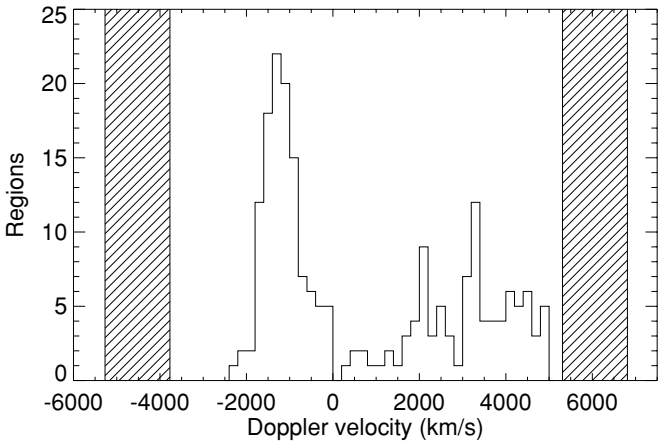

Figure 4. Velocity distribution of [Si II] emission interior to the bright ring. Hatched regions represent the expected velocities (−4520, +6061 km s^{-1}) and the velocity width (1500 km s^{-1}) of the reverse shock at the remnant's center (Reed et al. 1995).

4.1. Electron Density

We can probe the change in density of the ejecta as they encounter the reverse shock using the [S III] lines. A temperature-insensitive density diagnostic is available in the 18.71 μm/33.48 μm ground-state fine structure doublet line ratio, arising from low-lying collisionally excited levels. Recovering electron density requires balancing the rates of collisional excitation and de-excitation and radiative transitions into and out of the relevant levels of the ion. For ions with p^2, p^3, and p^4 ground state electron configurations, like S^{++}, it is sufficient to consider only the five lowest lying energy levels (Osterbrock & Ferland 2006). Up to date temperature-dependent collisional rates were taken from the IRON project (Hummer et al. 1993) using its TIPBASE database interface. Radiative rates were obtained either from the IRON project, or, where available and reliable, from the NIST Atomic Spectra Database.[8] The five coupled linear rate equations were solved numerically for all level populations, imposing the constraint that the population fractions sum to unity. This solution is performed for a given temperature and density, interpolating the temperature-dependent collisional rates over log(T). The resulting line ratio dependence on density is illustrated in Figure 5. The [S III] 18 μm/[S III] 33 μm line ratio saturates in the high density limit at 11.9, when collisions are rapid enough to populate the levels in equilibrium according to their statistical weights, and at a low density limit of 0.56, when radiative effects dominate.

[8] http://physics.nist.gov/PhysRefData/ASD/

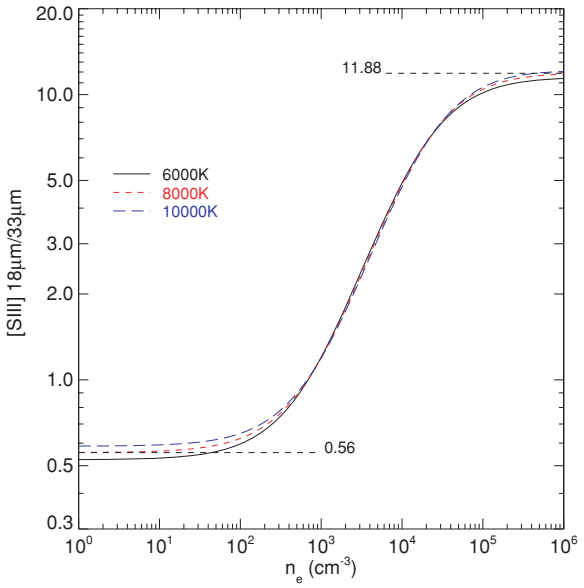

Figure 5. [S III] 18 μm/[S III] 33 μm density diagnostic for three representative temperatures.

(A color version of this figure is available in the online journal.)

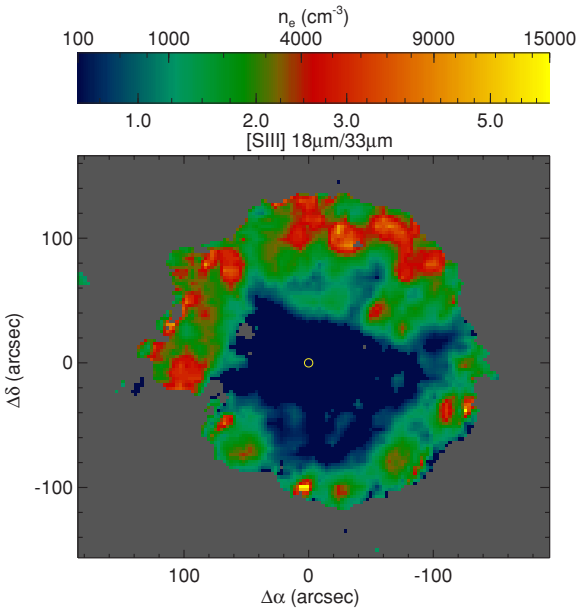

Figure 6. Electron density in the remnant, computed from the [S III] 18 μm/[S III] 33 μm ratio. Regions without sufficient signal in the ratio map are shown gray. The darkest regions, which include most of the interior emission, are in the low density limit of $n_e \lesssim 100$ cm^{-3}. The expansion center position of Thorstensen et al. (2001) is marked as a small circle, with offsets relative to it.

(A color version of this figure is available in the online journal.)

To recover electron density in the remnant, the two [S III] line maps were spatially registered and convolved to matching resolution using a custom convolution kernel constructed from *Spitzer's* TinyTim point-spread function models in the manner of Gordon et al. (2008). The matched images were then ratioed, and corrected for $A_V = 5$ magnitudes of extinction using the interstellar extinction curve of Chiar & Tielens (2006; which results in a modest 10% increase). All data in the ratio map with signal to noise below 2.25 were discarded, and map regions within 1σ of the low or high-density ratio limits were set to the limiting densities.

The [S III] 18 μm/[S III] 33 μm ratio ranges from 0.5 near the center to a maximum of 7.5 on the bright rim. The resulting projected density map is shown in Figure 6. This density is averaged over spatial scales of 10″ (0.16 pc). Although the bright ring is not generally confused by overlapping Doppler components at this spatial resolution (Lawrence et al. 1995), high-resolution optical and X-ray images resolve structure out at 0.″2–1″ (Hughes et al. 2000; Fesen et al. 2001), so even without projection effects, some blending of structure is unavoidable. In regions where two or more strong emission components are present along the line of sight, which includes most of the interior emission, the [S III] line ratio represents the emission-weighted average electron density. However, individual line ratios calculated for red- and blueshifted [S III] line sets in the interior emission near the remnant center yielded consistent values of ~ 0.5.

The interior [S III] emission is uniformly in or near the low limiting density of the [S III] diagnostic ($n_e \lesssim 100$ cm^{-3}), whereas the electron density in gas compressed by the reverse shock is much higher, peaking above 1.5×10^4 cm^{-3}. This general result holds even assuming much lower temperatures, down to 1000 K. Unshocked interior emission at much lower densities has also been observed in the type Ia supernova remnant SN1006 (e.g., Hamilton & Fesen 1988), and were originally identified in Cas A through free-free absorption of low frequency radio emission by Kassim et al. (1995). Hurford & Fesen (1996) obtain densities ranging from 5000 to 15,000 cm^{-3} for a range of optical knot compositions, consistent with Chevalier & Kirshner (1979), and in good agreement with our results on the bright rim.

Since the density enhancement in strong nonradiative shocks is limited to a factor of four, the strong density enhancement provides evidence for rapid radiative cooling of the infrared emitting clumps after they pass through the shock. Alternatively, hidden dense clumps may be entrained in the outflowing material, which are illuminated only as they pass through the shock. This could then represent an extension to higher densities of the clumpiness apparent in the more diffuse X-ray-emitting ejecta (Morse et al. 2004).

4.2. Ionization State

The progression of the reverse shock into the ejecta can be observed not only in the electron density, which increases by at least two orders of magnitude, but also in the ionization state of the outflowing atomic material as it encounters the reverse shock.

Figure 7 illustrates this progression by comparing line maps from two infrared lines arising from ions of differing ionization potential—[Si II] (8.2 eV) and [S IV] (34.8 eV)—together with a summed pair of high-energy X-ray helium-like and hydrogen-like K-alpha resonance lines: Si XIII (0.5 keV) and Si XIV (2.4 keV; Hwang et al. 2000). There is clear layering of ionization state, from low energy species in the interior, higher energies on the bright ring where optical emission is also seen, and very high energies traced by X-ray line emission extending beyond the infrared-bright rim itself. Though line of sight projection of multiple structures complicates the view in the northern rim, it is evident that the *observed* layering is highly nonuniform as a function of azimuth as well as along the line of sight.

In various positions, more or less of the O-burning layer has encountered the reverse shock. In the direction along our line of sight, very little of this material has reached the shock.

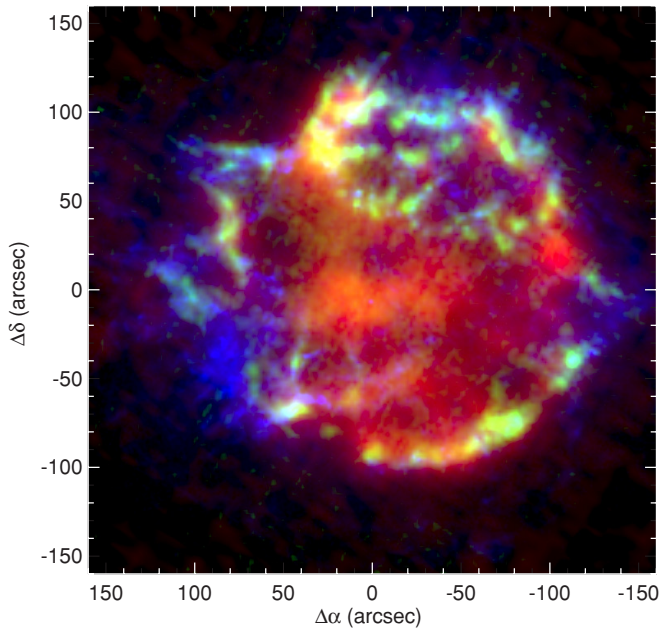

Figure 7. Color-coded map in [Si II] 34.8 μm (red, ionization energy 8.2 eV), [S IV] 10.5 μm (green, ionization energy 34.8 eV), and the summed X-ray emission of Si XIII+Si XIV (hydrogen- and helium-like silicon, blue, ionization energy 0.5–2.4 keV). Square-root scaling is used for all three channels, and the coordinate scale follows Figure 2, with a 320″ image size. Immediately evident is the inside-out layering of ionization state, with low-energy species in the unshocked interior region, and higher-energy species layered within the nonuniform shock region itself.

(A color version of this figure is available in the online journal.)

These regions are dominated by low ionization lines, [Si II] in particular (see Figure 7), which lie at lower velocities than the shocked ring of emission (Figure 4). In these directions, neither element is seen in higher ionization states in the infrared or X-ray. This low ionization pattern also appears at different azimuths along the bright ring, indicative of positions where O-burning ejecta moving approximately in the plane of the sky have yet to encounter the reverse shock. This emission is consistent with material inside the reverse shock which has been ionized by ambient Galactic stellar radiation and/or illumination from the rim of shocked ejecta.

In other directions, moderate ionization state material traced by [S IV] is present, with weak or absent X-ray emission. Finally, there are regions where only the high ionization Si X-ray lines are seen, predominantly at large radii. These variations likely represent different stages in the postshock histories of the inhomogeneous ejecta. The low density X-ray filaments and diffuse material are gradually heated and ionized as they penetrate the reverse shock, with a time history that depends on the shape of the ejecta density profile (Laming & Hwang 2003). Higher density clumps of material can suffer a different fate, reaching temperatures of only $\sim 10^4$ K as they undergo rapid radiative cooling immediately postshock, and are seen in [S IV].

The detailed histories of shock-heated material requires considerably more modeling, which incorporates variations in ejecta density and its profile, ejecta velocities, and irregularities in the location of the reverse shock. It is not clear to what degree the density and ionization state of the material we now see passing through the shock front is determined by initial conditions of the ejecta—diffuse versus clumpy, lower versus higher velocity—and to what degree the heating, photo- and collisonal ionization, and subsequent cooling by line radiation redistributes material between these phases. What is clear, however, is that the ejecta undergo a striking and rapid change in density and ionization level as they encounter the reverse shock.

5. APPARENT INHOMOGENOUS MIXING AND THE NEON CRESCENTS

The Cas A ejecta are by no means homogenous in composition or uniform in their layering. Using optical spectroscopy, Chevalier & Kirshner (1979) demonstrated abundance inhomogeneities in the oxygen burning products S, Ar, and Ca among the outlying fast moving knots, and suggested differing completeness levels of oxygen burning could explain these variations. Macroscopic mixing of similar nucleosynthetic products was suggested by Douvion et al. (1999) using ISO MIR line maps of Ar, Ne, and S covering a portion of the bright rim. Hughes et al. (2000) used Chandra X-ray spectroscopy to identify spatial inversion of iron and oxygen burning products. It would be fair to say that nonuniformity of composition is the rule rather than the exception in Cas A.

In a stratified model in which different layers of ejecta material are coming into contact with the reverse shock front in different directions, the appearance of individual emission lines depends on (1) the expansion velocity of material, (2) the position of the reverse shock with respect to it, and (3) the subsequent ionization state of the material as it passes through the shock. In this context, even if the gross nucleosynthetic layering is preserved in the outflow, with lighter elements overlying heavier ones, differing outflow velocities in different directions can generate an *apparent* mixing of layers, since different strata are now arriving at and passing through the reverse shock boundary in different regions. Combined with line of sight projection effects, this can profoundly complicate interpretation of apparent elemental mixing, a conclusion also drawn in the jet-induced explosion model of Wheeler et al. (2008).

A powerful example of this apparent mixing is found in the neon maps. Neon is among the most abundant elements in the carbon and oxygen shell-burning cores of intermediate mass supernovae progenitors (Meakin & Arnett 2006). In contrast to the optical neon lines, which are highly obscured by line of sight extinction, and therefore difficult to study (e.g., Chevalier & Kirshner 1979; Fesen 1990), the MIR neon lines are bright and readily detected throughout the ejecta ring.

A three color composite image of [Ar III], [S IV], and [Ne II] in Figure 8 reveals two bright, crescent-shaped clumps of highly enhanced neon abundance to the north and south along the ring. Lines of Ar, Si, and S are very faint in these regions, and they have excess 4.5 μm brightness (Ennis et al. 2006). The blended complex [O IV]+[Fe II] is strong as well, though the coarser angular resolution prevents completely separating the small regions from the surrounding ring material at these longer wavelengths.

The [Ne II]/[Ar III] ratio changes dramatically—from 0.8 $\pm$ 0.4 on the rim outside of these crescent regions, to over 50 on the crescents themselves. Since the remnant regions occupied by the Ne crescents are not overly confused by overlapping Doppler structures (Lawrence et al. 1995), the large ratio differences represent real abundance variations. Variations in abundance from optical emission lines of S and O are also observed at spatial resolutions of 1″ (Reed et al. 1995) and down to individual ejecta knots at the 0.″2 level (Fesen et al. 2001).

Overlaid on the image are the remnant expansion center of Thorstensen et al. (2001) as well as the location of the

Table 2
Neon Crescent Line Fluxes

Name	Position (J2000)	Area (pc^2)	$F_{[Ne\ II]}$ [a]	$F_{[Ne\ III]}$ [a] (10^{-15} W m^{-2})	$F_{[Ne\ V]}$ [a]	M_{Ne} [b] ($10^{-5}\ M_\odot$)
Ne South	23:23:31.53 + 58:47:22.6	0.33	15.9 ± 0.04	5.59 ± 0.06	<0.09[c]	8.9 ± 0.4
Ne North	23:23:25.88 + 58:50:07.2	0.21	16.9 ± 0.04	5.62 ± 0.05	0.735 ± 0.02	9.7 ± 0.5

Notes.
[a] Corrected for $A_V = 5$ magnitudes of extinction. Statistical uncertainties only. Additional systematic uncertainties apply (∼10% for [Ne II], [Ne III]; ∼25% for [Ne V]).
[b] Excluding neutral neon.
[c] 3σ upper limit.

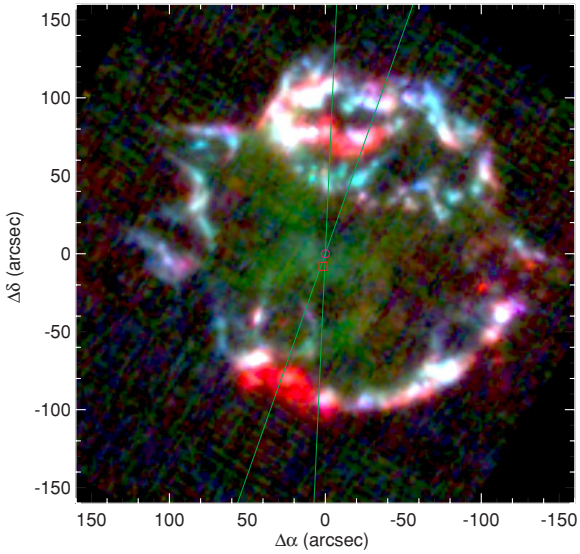

Figure 8. Composite image of [Ar III] (blue), [S IV] (green), and [Ne II] (red), showing two pronounced neon-rich crescent-shaped regions to the N and S (square-root scaling). Axes as Figure 7. Also shown are the kinematic center of the remnant (magenta circle, Thorstensen et al. 2001) and X-ray localization of the remnant's compact object (red square, 7″ to the south). Green lines indicate the 1σ range of the "kick vector" direction of the compact object from the ejecta's expansion center: 169°± 8.4° (Fesen et al. 2006). The two regions of enhanced neon abundance lie very close to this projected direction. Several much smaller neon-enhanced regions lie in the west along the X-ray jet direction.

(A color version of this figure is available in the online journal.)

X-ray compact object, which is offset from the kinematic center by ∼7″ to the south. The projected direction of motion, representing the asymmetric kick received by the compact object, is 169°± 8.4° (Fesen et al. 2006). The symmetric neon crescents lie nearly perfectly along this kick direction. Though the true-space velocity of relative motion between the compact object and kinematic center is unknown, this strongly suggests a preferred axis of symmetry in the outflow along this direction.

Of obvious interest is the total emitting mass of neon in the crescents. The observed line flux F of a collisionally excited emission line is

$$F = \frac{h\nu A_{ul}}{4\pi d^2} \int_V f_u n_{\rm ion} dV, \quad (1)$$

where A_{ul} is the radiative rate between the two levels involved in the emission, f_u is the fractional population of the upper level, $n_{\rm ion}$ is the ion density, V is the physical volume over which the emission occurs, and d is the distance. Assuming the fractional density of the ion is constant over the emission volume, the emitting mass of the ion is therefore

$$M_{\rm ion} = m_{\rm ion} n_{\rm ion} V = \frac{4\pi d^2 F}{A_{ul} f_u h\nu} m_{\rm ion}, \quad (2)$$

where $m_{\rm ion}$ is the atomic mass. We take a representative electron density on the bright rim of $n_e = 4500$ cm^{-3} from the [S III] analysis of Section 4.1, and bracket our uncertainty in the temperature by adopting $T = 5500$–8000 K (see Hurford & Fesen 1996). Isolating the regions of elevated [Ne II]/[Ar II] using polygonal apertures, we obtain the integrated fluxes for the crescents indicated in Table 2. Each crescent is approximately 0.25 pc^2 in size, and contributes roughly 10% of the remant's total [Ne II] line flux. The [Ne III] line is also relatively strong in each crescent region, but [Ne V] is very faint and not seen in the Southern crescent. The [Ne V]/[Ne II] ratio in the northern crescent is $\gtrsim 8\times$ that of the Southern region, although the velocity difference between the two lines at that position is $\gtrsim$ 1000 km s^{-1}, suggesting that the increased line of sight confusion in the Northern cap may play a role in this discrepancy. Ne^{4+} contributes negligibly to the mass.

Assuming they emit in similar volumes, the densities of Ne^{++} and Ne^{4+} relative to Ne^{+} can readily be estimated by forming a ratio of Equation (1) for each of the higher ionized species to the lower, which eliminates all quantities except the line flux, upper level population, radiative rate, and frequency. We solve for the level populations using atomic data for neon obtained and applied in the manner described in Section 4.1. This results in $n_{Ne^{++}}/n_{Ne^{+}} = 0.17$ in both regions, and, in the north, $n_{Ne^{4+}}/n_{Ne^{+}} = 0.003$. Assuming these ions are the dominant source of electrons, and taking the fractional density of the unseen ion Ne^{+++} (which does not emit in the MIR) as 0.05, we can estimate

$$\frac{n_e}{n_{Ne^{+}}} = 1 + 2\frac{n_{Ne^{++}}}{n_{Ne^{+}}} + 3\frac{n_{Ne^{+++}}}{n_{Ne^{+}}} + 4\frac{n_{Ne^{4+}}}{n_{Ne^{+}}} \approx 1.5. \quad (3)$$

Using Equation (2) to calculate the mass, we find roughly $1.8 \times 10^{-4}\ M_\odot$ of neon in the crescent regions (dominated by Ne^{+} and Ne^{++}, and excluding neutral neon). This mass is comparable to that found by Arendt et al. (1999) in other (larger) segments of the rim. The entire ionized neon mass of the remnant, assuming an approximately constant density throughout the bright rim, is $8.6\times10^{-4}\ M_\odot$, such that roughly 20% of the neon mass is concentrated in two small regions covering $\lesssim$2% of the rim's area.

The relative abundance of Ne to Ar (neglecting neutral species of both) can be calculated using line maps of [Ar II] and [Ar III]. We assume the same temperature and densities used for neon, and calculate level populations as above. The relative abundance increases from $n_{\rm Ne}/n_{\rm Ar} = 2.7$ averaged over the full remnant to

$n_{Ne}/n_{Ar} = 26$ on the S crescent region. These likely represent lower limits on the full relative abundance, including neutral species, as the first ionization potential of Ne (21.6 eV) is substantially larger than that of Ar (15.8 eV), so that the average neutral fraction can be assumed to be larger in the former.

Flowing outward ~ 20 degrees from the plane of the sky at roughly -5500 km s^{-1} (south) and +4200 km s^{-1} (north; see T. DeLaney et al. 2009, in preparation), the ionized neon moving in these crescent-shaped clumps represent only 4×10^{-5} of the estimated 10^{44} J of expansion energy in the entire remnant (Willingale et al. 2003). Assuming the neutron star is moving in the plane of the sky, the 7.″0 separation it has obtained from the expansion center since the explosion (Fesen et al. 2006) implies a velocity of 342 km s^{-1}. Further assuming it to have a mass of $\sim 1.4\ M_{\odot}$ (e.g., Young et al. 2006), the momentum impulse imparted by the kick to the neutron star is then $\gtrsim 1000\times$ larger than that of either neon crescent.

Since they represent such small fractions of the full ejecta's kinetic energy and the momentum of the neutron star, it is unlikely that even a very large asymmetry in the neon crescents' initial velocities could have directly contributed to the kick experienced by the compact object with respect to the expanding ejecta. In many ways, however, the infrared emitting mass of neon in the crescents must be a significant underestimate of the full column of material moving along this symmetric pair of directions, with layers of heavier elements which have not yet reached the reverse shock still largely unilluminated, neutral species missing from the estimate, hotter X-ray gas at greater radii, and other elements such as oxygen entrained in the crescents themselves not readily accounted for.

In the final shell burning nucleosynthetic structure, the neon layer lies above the heavier silicon, sulfur, and argon layers (Woosley & Weaver 1995). If the gross layering of pre-explosion elements is preserved, the strong overabundance of neon in these crescents along the direction of the kick vector could in fact represent material which is *late* in meeting the reverse shock, having been accelerated to slightly slower initial speeds. If so, it could be expected that the neon will gradually become less dominant as it progresses further beyond the shock and cools, with sulfur and argon filling in behind it. In this sense, this pair of directions is intermediate between the bright rim, cooling dominantly in lines of Ar, and the front and back surfaces along the line of sight, along which very little material has yet encountered the reverse shock.

The fact that the compact neon crescents are nearly equal in size and in mass, and are arranged symmetrically about the expansion center, strongly indicates they arise not from macroscopic or turbulent mixing of the ejecta layers during expansion, but from a preferred axis in the initial outflow configuration along this direction.

6. CONCLUSIONS

We present global low-resolution 5–37 μm spectral maps of the Cas A supernova remnant obtained with *Spitzer*'s IRS spectrograph. We detect numerous fine-structure emission lines arising from ions with ionization energies of 8–100 eV, and strengths that vary considerably across the remnant. The observed ions represent some of the most abundant species in oxygen and carbon shell burning supernova progenitor cores. We find the following.

1. Strong interior emission of predominantly low-ionization, heavy ionic species, dominated by [Si II]. These regions lie inside the bright rim along the line of sight, and probe slower moving material which has cooled from the passage of the initial outgoing forward shock wave, but which has not yet encountered the reverse shock.
2. The electron density in the remnant increases rapidly from $\lesssim 100$ cm^{-3} in the unshocked interior to $\sim 10^4$ cm^{-3} on the bright ring of emission, indicative of rapid cooling of material passing through the shock front, or significant preshock density inhomogeneity.
3. The ionization state increases rapidly as the ejecta encounter the reverse shock, with low-ionization species dominating inside the shock, moderate-ionization species strongest just outside the shock, and very high-ionization material seen in X-rays at the greatest distances. These variations in postshock history may depend on the density structure of the inhomogenous ejecta.
4. Two symmetrically arranged, compact, crescent-shaped clumps of material with highly enhanced neon abundance (greater than $10\times$ the remnant average) lie along the projected direction of the "kick vector" separating the compact object from the expansion center of the remnant, tracing a new axis of explosion asymmetry in the ejecta. Since neon is expected to arrive at the reverse shock before heavier elements like Si and S, these could represent directions of *reduced* initial velocity, intermediate between the bright rim, and the (still) quiescent material flowing toward the front and back faces of the remnant, which has yet to reach the reverse shock.
5. Since the ionization state and density vary steeply with distance from the expansion center, and have such a strong impact on the observed strength of individual emission lines, the apparent macroscopic mixing of elements in Cas A may result from variations in initial outflow velocity rather than bulk turbulent redistribution of the ejecta strata. The symmetry in mass and outflow direction of the neon crescent regions strongly supports this interpretation.

The authors thank D. Arnett for helpful discussion, and an anonymous referee for useful comments which improved this manuscript. This work is based on observations made with the *Spitzer Space Telescope*, which is operated by the Jet Propulsion Laboratory, California Institute of Technology under NASA contract 1407. Support for this work was provided by NASA/JPL through award 1264030.

REFERENCES

Albert, J., et al. 2007, A&A, 474, 937
Arendt, R. G., Dwek, E., & Moseley, S. H. 1999, ApJ, 521, 234
Chevalier, R. A., & Kirshner, R. P. 1979, ApJ, 233, 154
Chiar, J. E., & Tielens, A. G. G. M. 2006, ApJ, 637, 774
DeLaney, T., & Rudnick, L. 2003, ApJ, 589, 818
Douvion, T., Lagage, P. O., & Cesarsky, C. J. 1999, A&A, 352, L111
Ennis, J. A., Rudnick, L., Reach, W. T., Smith, J. D., Rho, J., DeLaney, T., Gomez, H., & Kozasa, T. 2006, ApJ, 652, 376
Fesen, R. A. 1990, AJ, 99, 1904
Fesen, R. A., Morse, J. A., Chevalier, R. A., Borkowski, K. J., Gerardy, C. L., Lawrence, S. S., & van den Bergh, S. 2001, AJ, 122, 2644
Fesen, R. A., et al. 2006, ApJ, 645, 283
Gordon, K. D., Engelbracht, C. W., Rieke, G. H., Misselt, K. A., Smith, J.-D. T., & Kennicutt, Jr, R. C. 2008, ApJ, 682, 336
Gotthelf, E. V., Koralesky, B., Rudnick, L., Jones, T. W., Hwang, U., & Petre, R. 2001, ApJ, 552, L39
Hamilton, A. J. S., & Fesen, R. A. 1988, ApJ, 327, 178
Hines, D. C., et al. 2004, ApJS, 154, 290
Houck, J. R., et al. 2004, ApJS, 154, 18

Hughes, J. P., Rakowski, C. E., Burrows, D. N., & Slane, P. O. 2000, ApJ, 528, L109
Hummer, D. G., Berrington, K. A., Eissner, W., Pradhan, A. K., Saraph, H. E., & Tully, J. A. 1993, A&A, 279, 298
Hurford, A. P., & Fesen, R. A. 1996, ApJ, 469, 246
Hwang, U., Holt, S. S., & Petre, R. 2000, ApJ, 537, L119
Kassim, N. E., Perley, R. A., Dwarakanath, K. S., & Erickson, W. C. 1995, ApJ, 455, L59
Kim, Y., Rieke, G. H., Krause, O., Misselt, K., Indebetouw, R., & Johnson, K. E. 2008, ApJ, 678, 287
Krause, O., Birkmann, S. M., Usuda, T., Hattori, T., Goto, M., Rieke, G. H., & Misselt, K. A. 2008, Science, 320, 1195
Lagage, P. O., Claret, A., Ballet, J., Boulanger, F., Cesarsky, C. J., Cesarsky, D., Fransson, C., & Pollock, A. 1996, A&A, 315, L273
Laming, J. M., & Hwang, U. 2003, ApJ, 597, 347
Lawrence, S. S., MacAlpine, G. M., Uomoto, A., Woodgate, B. E., Brown, L. W., Oliversen, R. J., Lowenthal, J. D., & Liu, C. 1995, AJ, 109, 2635
Meakin, C. A., & Arnett, D. 2006, ApJ, 637, L53
Morse, J. A., Fesen, R. A., Chevalier, R. A., Borkowski, K. J., Gerardy, C. L., Lawrence, S. S., & van den Bergh, S. 2004, ApJ, 614, 727
Osterbrock, D. E., & Ferland, G. J. 2006, Astrophysics of Gaseous Nebulae and Active Galactic Nuclei (2nd. ed.; Sausalito, CA: Univ. Sci. Books)
Reed, J. E., Hester, J. J., Fabian, A. C., & Winkler, P. F. 1995, ApJ, 440, 706
Rho, J., et al. 2008, ApJ, 673, 271
Rudnick, L. 2002, in ASP Conf. Ser. 262, The High Energy Universe at Sharp Focus: *Chandra* Science, ed. E. M. Schlegel & S. Vrtilek (San Francisco: CA: ASP), 293
Smith, J. D. T., et al. 2007, PASP, 119, 1133
Thorstensen, J. R., Fesen, R. A., & van den Bergh, S. 2001, AJ, 122, 297
Werner, M. W., et al. 2004, ApJS, 154, 1
Wheeler, J. C., Maund, J. R., & Couch, S. M. 2008, ApJ, 677, 1091
Willingale, R., Bleeker, J. A. M., van der Heyden, K. J., & Kaastra, J. S. 2003, A&A, 398, 1021
Woosley, S. E., Pinto, P. A., Martin, P. G., & Weaver, T. A. 1987, ApJ, 318, 664
Woosley, S. E., & Weaver, T. A. 1995, ApJS, 101, 181
Young, P. A., et al. 2006, ApJ, 640, 891